Published in final edited form as:

J Am Chem Soc. 2021 June 02; 143(21): 8193–8207. doi:10.1021/jacs.1c03572.

Remarkable, Unexpected Mechanism for (*S*)-3-Amino-4-(Difluoromethylenyl)cyclohex-1-Ene-1-Carboxylic Acid as a Selective Inactivator of Human Ornithine Aminotransferase

Wei Zhu[†,a], **Peter F. Doubleday**[†,b], **Arseniy Butrin**[†,c], **Pathum M. Weerawarna**[a], **Rafael Melani**[b], **Daniel S. Catlin**[c], **Timothy A. Dwight**[a], **Dali Liu**[*,c], **Neil L. Kelleher**[*,a,b], **Richard B. Silverman**[*,a,b,d]

[a]Department of Chemistry, Chemistry of Life Processes Institute, Center for Molecular Innovation and Drug Discovery, and Center for Developmental Therapeutics, Northwestern University, Evanston, Illinois 60208, United States

[b]Department of Molecular Biosciences, Northwestern University, Evanston, Illinois 60208, United States

[c]Department of Chemistry and Biochemistry, Loyola University Chicago, Chicago, Illinois 60660, United States

[d]Department of Pharmacology, Northwestern University, Chicago, Illinois 60611, United States

Abstract

Human ornithine aminotransferase (*h*OAT) is a pyridoxal 5′-phosphate (PLP)-dependent enzyme that was recently found to play an important role in the metabolic reprogramming of hepatocellular carcinoma (HCC) *via* proline and glutamine metabolic pathways. The selective inhibition of *h*OAT by compound **10** exhibited potent *in vivo* antitumor activity. Inspired by the discovery of aminotransferase inactivator (1*S*,3*S*)-3-amino-4-(difluoromethylene)cyclopentane-1-carboxylic acid (**5**), we rationally designed, synthesized, and evaluated a series of six-membered ring analogs. Among them, **14** was identified as a new selective *h*OAT inactivator, which demonstrated 22 times greater potency than **10**. Three different types of protein mass spectrometry and two crystallographic approaches were employed to identify the structure of *h*OAT-**14** and the formation of a remarkable final adduct (**28`**) in the active site. These spectral studies reveal an enzyme complex, heretofore not observed in a PLP-dependent enzyme, with covalent bonds

---

[*]Corresponding authors (R.B.S.) Agman@chem.northwestern.edu. Phone: +1-847-491-5653, (N.L.K.) n-kelleher@northwestern.edu. Phone: +1-847-467-4362. (D.L.) dliu@luc.edu. Phone: +1-773-508-3093.

[‡]**Present Addresses** P.F.D.: Institute of Molecular Systems Biology, ETH Zurich, 8093 Zurich, Switzerland.

[†]W.Z., P.F.D., and A.B. contributed equally to this paper.

ASSOCIATED CONTENT

Supporting Information

Supporting Information is available free of charge on the ACS Publications website. Supplementary figures and tables, experimental methods, syntheses, spectra, and crystallographic data.

Accession Codes

Atomic coordinates and corresponding structure factors for the soaking result and cocrystal complex have been deposited at the Protein Data Bank (PDB) as 7LOM, 7LON and 7LNM, respectively. Authors will release the atomic coordinates upon article publication.

The authors declare no competing financial interest.

to two nearby residues. Crystal soaking experiments and molecular dynamics simulations were carried out to identify the structure of active site intermediate **27`**, and to elucidate the order of the two covalent bonds formed, leading to **28’**. The initial covalent reaction of the activated warhead occurs with *Thr322 from the second subunit, followed by a subsequent nucleophilic attack by catalytic residue Lys292. The turnover mechanism of **14** by *h*OAT also was supported by mass spectrometric analysis of metabolites and fluoride ion release experiments. This novel mechanism for *h*OAT with **14** will contribute to the further rational design of selective inactivators and an understanding of potential inactivation mechanisms by aminotransferases.

Graphical Abstract

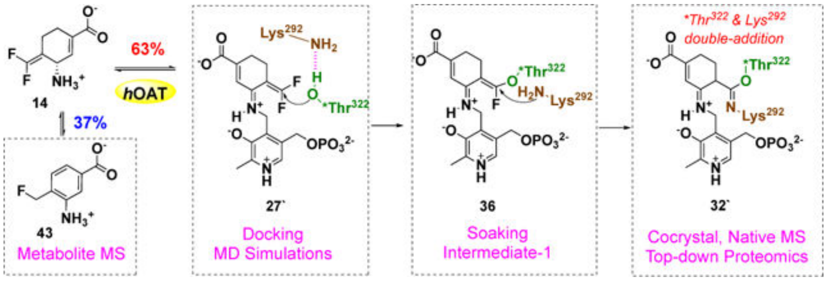

Keywords

Mechanism-based inactivators; Covalent inhibitors; Inactivation mechanism; Top-down proteomics; Human ornithine aminotransferase; Hepatocellular carcinoma

INTRODUCTION

Hepatocellular carcinoma (HCC) is the most common primary liver cancer and the second leading cause of cancer death worldwide.[1–4] The disease is highly malignant, radiotherapy-resistant, and refractory to chemotherapy, including the standard-of-care treatment, sorafenib.[5–8] Recently, human ornithine aminotransferase (*h*OAT) was identified as a metabolic regulator of HCC progression *via* proline and glutamine metabolic pathways.[9, 10] OAT (E.C. 2.6.1.13) is a pyridoxal 5′-phosphate (PLP)-dependent enzyme,[11] which is found in the mitochondrial matrix of most human and animal tissues.[12] Mechanistically, two coupled half-reactions are required to complete one transamination cycle of OAT (Scheme 1).[13] In the first half-reaction, ornithine binds to cofactor PLP in the active site of OAT to form Schiff base **M1**, followed by tautomerization to intermediate **M2**; the subsequent hydrolysis of **M2** generates pyridoxamine 5′-phosphate (PMP) and glutamate γ-semialdehyde (GγS), which spontaneously cyclizes to Δ^1-pyrroline-5-carboxylate (P5C). In the second-half reaction, OAT catalyzes the conversion of α-ketoglutarate (α-KG) and PMP to L-glutamate (L-Glu) and PLP. Glutamate and glutamine metabolism have acknowledged roles in supporting the anabolic demands of tumor growth and it is increasingly clear that proline metabolism promotes liver cancer tumorigenesis.[14–17] Not only L-Glu and proline have direct effects on metabolic rewiring, but they also induce a hypoxia-inducible factor-1α (HIF1α) transcriptional program in HCC leading to sorafenib resistance and retained proliferative capacity under oxygen starvation.[18] *h*OAT is commonly overexpressed in HCC as a result of dysregulation and activation of the Wnt/β-catenin pathway.[19, 20] The selective inhibition of *h*OAT exhibited potent *in vivo* anti-tumor activity in the HCC mouse model, along with dramatically reduced alpha-fetoprotein (AFP, a biomarker for HCC) levels.[10] Recently, upregulation of *h*OAT was found in non-small cell lung cancer (NSCLC) cells, which contributes to the promotion of proliferation, invasion, and migration, the inhibition of apoptosis, and the change of the cell cycle.[21] The specific knockdown of *h*OAT in NSCLC inhibited cell proliferation *in vitro* and suppressed tumor growth *in vivo*.[21] Thus, *h*OAT can serve as a promising therapeutic target for the treatment of HCC and related cancers with similar underlying metabolic alterations.

OAT belongs to the same enzyme subgroup[22] as γ-aminobutyric acid aminotransferase (GABA-AT, E.C. 2.6.1.19), which demonstrates a similar catalytic mechanism to that of OAT,[23] in which GABA is converted to succinic semialdehyde (SSA) in the first-half reaction.[24] In past decades, our laboratory has been focusing on the rational design of mechanism-based inactivators (MBIs) of GABA-AT[25] for the potential treatment of epilepsies and addictions. MBIs initially act as substrates for a target enzyme, but after enzyme-catalyzed modification to an active intermediate, they inhibit the target enzymes;[25–28] often they demonstrate higher potency and reduced off-target effects when compared with traditional inhibitors. [10, 25, 29, 30] Vigabatrin (**1**)[31], an MBI of GABA-AT, is an FDA-approved drug for the treatment of infantile spasms and refractory complex partial seizures (Scheme 2).[32] A mechanistic study[33] revealed that **1** initially forms a Schiff base with PLP in the active site of GABA-AT, followed by tautomerization, as with the native substrate, to afford intermediate **3**. Lys329, the residue that initially is bound to PLP, attacks the Michael acceptor of **3** to form covalent adduct **4**, which accounts for 70% of the inactivation pathway of **1** (Scheme 2).[33] On the basis of this mechanism, difluoro-substituted conformationally-rigid compound **5** was synthesized and exhibited 22 times higher efficiency as an inactivator of GABA-AT than **1**, determined by their k_{inact}/K_I values (Scheme 2).[34, 35] Compound **5** produced Michael acceptor intermediate **7** via similar steps as shown for the mechanistic pathway of **1**.[36] However, highly electrophilic **7** reacted with water molecules in the pocket, instead of Lys329, leading to the formation of tight-binding adduct **8**, in which the newly generated carboxylate forms an electrostatic interaction with Arg445 (Scheme 2).[36] Compound **5** has been investigated in a clinical trial and is successfully treating a child with infantile spasms.[37, 38] Cyclopentene analog **9** (Figure 1) was found to have enhanced improved potency toward GABA-AT ($k_{inact}/K_I = 342\ mM^{-1}min^{-1}$) and to undergo the same mechanism as **5**, in which the nucleophilic attack of water molecules was potentially assisted by the catalytic lysine.[29] Because of the high similarity of the active sites of these two aminotransferases, **9** also exhibited inhibitory activity of *h*OAT, but with relatively lower efficiency ($k_{inact}/K_I = 7.6\ mM^{-1}min^{-1}$).[29]

When comparing the active sites of *h*OAT and GABA-AT for differences, *h*OAT has a more flexible and larger active site, resulting from the replacement of Phe351 and Ile72 in GABA-AT with Tyr55 and Tyr85 in *h*OAT, which can accommodate ornithine that is one carbon longer than GABA.[39] In 2015, the relatively bulky bis(trifluoromethyl) analog **10** (Figure 1) was found to show much improved selectivity for *h*OAT over GABA-AT.[10] Furthermore, administration of **10** at low doses (0.1 and 1.0 mg/kg) was shown to effectively reduce AFP levels and suppress HCC tumor growth *in vivo.*[10] Recently, the enlarged-ring strategy has been successful in improving potency and selectivity of *h*OAT inactivators, leading to the discovery of cyclohexene analogs **11a** and **11b** (Figure 1).[40]

Herein, we have designed and synthesized six-membered ring analogs **12**-**15** based on GABA-AT inactivators **5** and **9** (Figure 1). Among them, analog **14** is 22 times more efficient as an inactivator of *h*OAT than **10**, along with excellent selectivity over other aminotransferases. We also elucidated the inactivation mechanism of **14** with the employment of several crystallography and mass spectrometry methods, leading to the identification of a remarkable, but unexpected, covalent adduct attached to two residues from two different chains in the *h*OAT active site. In addition, the turnover mechanism was shown to generate an aromatic metabolite. These studies have revealed a potent and selective *h*OAT inactivator for the treatment of HCC and uncovered its underlying mechanism of inactivation for further improved rational inactivator design.

RESULTS AND DISCUSSION

Syntheses of Analogs 12–15

The synthetic route to **12–15** is shown in Scheme 3. Chirally-pure lactam **16**[41] was prepared via a reported procedure. Intermediate **16** was treated with silver trifluoroacetate, followed by Dess-Martin oxidation, to afford ketones **17a** and **17b**. Intermediate **18** was obtained from **17b** with the protection of PMB, followed by the treatment[34, 35] of $CHF_2PO(OEt)_2$ and ^{t}BuLi, to provide intermediate **19**. Deprotection of PMB with CAN and the ring-opening reaction under acid conditions afforded the desired product **12**. Chirally-pure ester **21** was prepared as reported,[40] which was treated[42] with 2-$PySO_2CF_2H$ and ^{t}BuOK in DMF to give difluoromethylene intermediate **22**. Interestingly, the treatment of **22** with PhSeCl and KHMDS afforded bicyclic lactam **23** as the major product. The sequential Boc protection, ring-opening reaction, and oxidative elimination provided two isomers **24a** and **24b**. The desired products **13–15** were afforded from the corresponding esters under acid conditions, respectively.

Kinetic Studies of Analogs 12–15

As shown in Table 1, six-membered ring analogs **12–15** exhibited lower binding affinity to GABA-AT (greater K_I values) than **5** or **9**, which is consistent with our initial design strategy. The enlarged ring could potentially obstruct the initial binding with GABA-AT,[40] which has a relatively small and rigid active site.[39] Although cyclohexane analogs **12** and **13** showed enhanced selectivity for OAT, their potency was greatly decreased. The introduction of the double bond significantly increased their binding affinity to OAT, which may result from the reduced steric hindrance of cyclohexene.[40] α, β-unsaturated analog **14** is more potent than cyclohexene analog **15**, possibly because of the reduced acidity of the γ-position, which is critical for the tautomerization step and further inactivation.[25]

The most potent analog (**14**) is 22-fold more efficient ($k_{inact}/K_I = 20.0\ min^{-1}mM^{-1}$) as an inactivator of *h*OAT than **10** ($k_{inact}/K_I = 0.9\ min^{-1}mM^{-1}$) and has good selectivity over GABA-AT with lower efficiency constants ($k_{inact}/K_I = 0.3\ min^{-1}mM^{-1}$). Compound **14** also exhibited little or no inhibitory activity against alanine aminotransferase (Ala-AT) or aspartate aminotransferase (Asp-AT), even at 20 mM concentration (Figure S1). Currently, *in vitro* and *in vivo* studies of **14** are ongoing in our lab for the potential treatment of HCC and other related cancers.

Inactivation Mechanism for 14

MBIs of aminotransferases inactivate these enzymes through a variety of mechanistic pathways, manifested by the formation of covalent or tight-binding adducts occupying the active site.[25] On the basis of previous reports,[33,36,43, 44] two reasonable mechanistic pathways (*a* and *b*) for the *h*OAT inactivation by **14** are proposed (Scheme 4). Initially, Schiff base **25** is formed from **14** and the Lys-PLP complex similar to that for the native substrate (Scheme 1), followed by deprotonation at the γ-position to **26**. Mechanistic *pathway a* is similar to the mechanisms for **1** and **5** (Scheme 2), in which reactive Michael acceptor intermediate **27** is generated by protonation at the PLP-C4` position. Nucleophilic attack could then occur by water (Scheme 4, *pathway a1*) to give potential tight-binding adduct **28** or by Lys292 to give covalent complex **29**. The fluorine-substituted olefin in **29** could further react (either directly or via the ketenimine) with a water molecule to afford adduct **30** (Scheme 4, *pathway a2*). In addition to water, several other nucleophilic residues (Nu) are nearby in the active site of *h*OAT, such as Tyr55, Tyr85, Glu235, and *Thr322 from the other chain. Although these noncatalytic residues have never been reported to be covalently modified in any inactivation mechanism for aminotransferases, it is possible that **29** could further react with one of them, leading to the formation of double-addition adduct **32** (Scheme 4, *pathway a3*). Mechanistic *pathway b* is proposed based on the inactivation mechanism of *h*OAT by gabaculine (Scheme S1),[43, 44] a naturally occurring neurotoxin.[45] Intermediate **33** could be formed by protonation at the difluoromethylenyl group of intermediate **26**, followed by tautomerization via **34** to **35**, a stable aromatic adduct with the PLP, similar to the product of inactivation by gabaculine. To determine the most likely mechanism for the inactivation of *h*OAT by **14**, we carried out dialysis experiments, three types of protein mass spectral experiments, obtained a cocrystal structure and a soaking crystal structure, and conducted molecular docking and molecular dynamic simulation (MD) studies.

Dialysis

Previously, five-membered ring analogs **5** and **9** were identified as partially irreversible inhibitors of GABA-AT, leading to the formation of tight-binding adducts.[29, 30] Thus, time-dependent reactivation experiments of *h*OAT for cyclohexene analog **14** were carried out to determine if similar reversible components were also involved during the inactivation. After *h*OAT was treated with 0.6–2.0 equivalents of **14**, aliquots at different time intervals were taken and assayed for the return of enzyme activity. No matter how many equivalents of **14** were used, no enzyme activity was recovered, even after 91 h of dialysis (Figure S2), supporting a fully irreversible inhibition of *h*OAT.

Native Mass Spectrometry

To determine the mass of the potential covalent or tight-binding adduct in the active site of *h*OAT-**14**, we turned to native mass spectrometry (nMS), which preserves noncovalent substrate binding and protein quaternary structure.[46] To evaluate the applicability of nMS for the study of MBIs, native untreated *h*OAT, *h*OAT-**11b**[40], and *h*OAT-gabaculine[44] samples were first used as positive controls. In these cases, the active site would be occupied by an unstable covalent adduct, a stable covalent adduct, and a tight-binding adduct, respectively. Theoretical mass shifts for control samples were calculated on the basis of known mechanisms; *h*OAT-**14** mass shifts were calculated from the proposed inactivation pathways *a1*-*a3* and *b* (Scheme 4, Figure S3). Data for protein dimers were deconvoluted to generate average dimer mass values (Figure S4). The experimental mass difference per monomer was calculated from the observed average mass of the apo-*h*OAT dimer (92275.0 Da). As shown in Table 2, independent of the binding mechanism for control samples, the experimental adduct masses are consistent with their theoretical masses. Among the proposed adducts for *h*OAT-**14**, only adduct **32** from pathway *a3* (Scheme 4) shows a mass shift (378.1 Da) that matches the experimental result (378.3 Da), indicating the involvement of a second nucleophilic residue.

Intact Protein Mass Spectrometry in Denaturing Mode

Protein mass spectrometry has served as an efficient tool for the identification of covalent adducts in studies of inactivation of aminotransferases.[40,47, 48] The hydrolysis of unstable groups under acidic conditions, such as imine or enamine groups, has been observed with intact protein mass spectrometry to create masses that correspond to stable covalent adducts alone.[42] Accordingly, unstable adducts for **14** may suffer from similar hydrolysis and release of PMP or result in cleavage of newly formed covalent bonds with Lys292/Nu. As shown in Figure S5, adducts and their corresponding theoretical mass differences for pathways *a1*-*a3* and *b* are depicted with partial adduct loss. For the cases of pathway *a1* or *b*, no mass shift should be observed for tight-binding adduct **28** or **35.** A mass shift of +166.0 Da is expected with the hydrolysis of PMP from adduct **30** (pathway *a2*); a range of mass shifts per monomer (148.0–166.0 Da) is proposed for *pathway a3* arising from different degrees of hydrolysis of adduct **32**.

By intact protein mass spectrometry, native unmodified, dimeric *h*OAT presented a deconvoluted mass compatible with the monomeric protein under acidic spray conditions and reversed-phase nanocapillary high performance liquid chromatography (nano HPLC, Figure 2A). [40, 47] However, using the same analytical conditions, analysis of *h*OAT-**14** yielded a deconvoluted mass consistent with dimeric, cross-linked *h*OAT, accounting for 82% of the total protein abundance (Figure 2B/C), suggesting covalent attachments to two residues, each from a different monomer in complex. Relative to the low abundance, unmodified dimer mass seen in the control (92275.0 ± 1.3 Da), a 305.0 Da mass shift was observed for the *h*OAT-**14** species (92580.0 ± 2.1 Da) (Figure 2D). The observed mass shift is not consistent with any single adduct but may result from a mixture of adducts (296.1–314.1 Da) in pathway *a3* (Scheme 4, Figure S5). To determine if modified, monomeric *h*OAT could be rescued from the observed dimer, the nanoHPLC analytical column temperature was increased from 25 °C to 55 °C. Subsequent analysis of *h*OAT-**14** at 55 °C reduced the dimer to 33% relative abundance and increased the abundance of unmodified *h*OAT and two additional monomeric forms of the protein (46137.5 ± 1.0 Da; 46304.0 ±2.5 Da; 46470.0 ± 2.2 Da) (Figure 2C/E). The mass shifts of 166.5 Da and 332.5 Da observed for the two *h*OAT-**14** monomer might be single (166.0 Da) and double adducts (2 ×166.0 Da, 332.0 Da), each attached to a single chain (Figure 2E), which would be consistent with the hydrolysis of adducts in pathway *a3* (Scheme 4, Figure S5).

Top-down Mass Spectrometry

We next turned to tandem mass spectrometry (MS/MS) to fragment intact proteins and localize the **14**-induced adduct within the *h*OAT primary sequence. Fragmentation of *h*OAT-**14** was first assessed using electron transfer dissociation (ETD), as this method preserves weaker covalent interactions and cross-linked peptides, and minimizing further adduct loss was desirable in this study.[49, 50] ETD fragmentation of unmodified control *h*OAT gave a set of 54 *z*-type ions that were readily mapped to the primary sequence as C-terminus containing fragments. In contrast, ETD fragmentation of *h*OAT-**14** created a complex MS/MS (MS2) spectrum with only 6 *z*-type ions that all mapped to positions after Leu340 (Figure S6). ETD fragmentation of *h*OAT-**14** is not consistent with the expected MS2 spectra for a single amino acid modification and suggests a more complex adduct, possibly because of the cross-linking from two different chains as observed in the intact protein MS (Figure 2). Therefore, as a complementary fragmentation method, higher-energy collisional dissociation (HCD)[51] was applied to untreated control *h*OAT, *h*OAT-**11b**[40] as a positive control, and *h*OAT-**14** (Figure 3). HCD fragmentation of control *h*OAT generated *y199* and *y140* ions corresponding to the cleavage between Val240/Pro241 and Tyr299/Pro300. These ions were used as diagnostic fragments for residue adduction between Lys292 and the C- terminus (Figure 3B, Figure S7/S8). For *h*OAT-**11b**, a +366 Da mass shift was observed and could be mapped to *y199*, consistent with the reported adduct mass (Figure 3C).[40] Neither *y140* nor any other y-ions corresponding to the cleavage between Lys292 and Val339 were identified for *h*OAT-**11b**, possibly because of stabilizing interactions between **11b** and active site residues. Nonetheless, fragmentation of *h*OAT-**11b** benchmarked these top-down fragmentation methods and their utility to retain and localize adducts. For *h*OAT-**14**, an addition of 166 Da in mass was observed on both *y199* and *y140* fragment ions (Figure 3D, Figure S7/S8). Given the mass shift on *y140* and not for any subsequent *y*-type ions that report on more C-terminal residues (i.e., the *y101* and smaller *y*-type fragment ions), **14**-mediated adduction must occur between Pro300 and Glu338 (Figure 3D). Of the nucleophilic residues in the active site of *h*OAT (Tyr55, Tyr85, Glu235, Lys292, and *Thr322), only *Thr322 occurs in the above range.

Collectively, the mass spectrometry supports a pathway where *h*OAT inactivated by **14** produces a covalent, dimeric protein complex, with modification of *Thr322. Native mass spectrometry studies support *h*OAT-**14** adduction between *Thr322 and Lys292, leading to adduct **32** within ±1 Da mass accuracy for the protein dimer. This study also suggests that loss of the adduct occurs as a result of imine hydrolysis[47, 48] under the acidic conditions of intact protein MS. Indeed, using a technique we previously developed,[42] we could detect PMP as the adduct cofactor following untargeted metabolomics of the flowthrough from fully inactivated, previously desalted hOAT-**14**, treated with trifluoroacetic acid at 37 °C

(Figure S9). A similar loss of adduct cofactor was previously observed when an imine bond was present.[42] Together, native mass spectrometry and top-down mass spectrometry serve as tools to directly readout molecular details and thereby help the future investigation of MBI characterization.

Cocrystal structure of *h*OAT Inactivated by 14

Although the mass spectrometry strongly indicated the formation of adduct **32** (pathway *a3*, Scheme 4) in the active site of *h*OAT when inactivated by **14**, top-down MS/MS was able to provide direct evidence for the covalent attachment to *Thr322 but not to catalytic residue Lys292. Hence, protein crystallography of *h*OAT inactivated by **14** was employed to interpret the adduct formed in the active site. The cocrystal structure of *h*OAT inactivated by **14** was solved by molecular replacement using a monomer from a previously reported structure of *h*OAT[53] (PDB code 1OAT), while water and ligand molecules were deleted. The refined model is shown in Figure 4: two covalent bonds are formed with Lys292 and *Thr322 of the other protein subunit, which is consistent with the mass spectrometry studies. The carboxylate group of the final adduct is located in proximity to Tyr55 with the formation of two hydrogen bonds. A similar arrangement is observed in the cocrystal structure of *h*OAT-**11b**. Considering the relative stability of the internal double bonds, adduct **32** was proposed initially, but tautomer **32`** (Scheme S2), with an external double bond, was built in the model based on its better fit to the $2F_o$-$F_c$ map after refinement (Figure 4). Although the resolution of the cocrystal (1.95Å) does not allow a definitive conclusion regarding the enantiomeric form of **32`**, the *R*-isomer was built into the model on the basis of its lower R_{free} factor and better fit to the omit map.

Previously, several *h*OAT inactivators[40, 47, 54, 55] were found to form a covalent bond with Lys292, but no inactivator has been found to covalently interact with *Thr322 or any other noncatalytic residues. Given the surprising involvement of *Thr322 during the inactivation process, a multiple sequence alignment was performed for 223 manually annotated and reviewed ornithine aminotransferase enzymes. By this analysis, we find that the active site residue Lys292 and *Thr322 are conserved throughout evolutionary history down to *E. coli*, suggesting a conserved functional role for these residues (Figure S10A). In contrast, a similar analysis of 18 known human PLP-dependent aminotransferases (EC 2.6.1) demonstrated that Thr322 is poorly conserved across this family of aminotransferases in humans (Figure S10B). Catalytic residue Lys292 plays an important role in the protein native reaction, which is covalently bonded to PLP and located close to *Thr322 (3.8 Å), as shown in the holoenzyme structure of *h*OAT (Figure S11A). Cocrystal[44] structures of *h*OAT with gabaculine (PDB: 1GBN, Figure S11B) and L-canaline (PDB: 2CAN, Figure S11C) reveal a potential hydrogen bond between the free Lys292 and *Thr322 (2.8 Å), indicating *Thr322 could be “activated” during the native reaction or inactivation process.

Intermediate **27** was proposed to be the active Michael acceptor for the inactivation process, whose difluoromethylene warhead is positioned near the internal H-bond between the protonated imine and oxygen anion (Scheme 4). Surprisingly, the *h*OAT-**14** complex demonstrates that the newly formed covalent linkage is moved to the phosphate side (Figure 4), suggesting an imine isomerization[56–59] of the intermediate during the inactivation process. Arg413 is known to form a salt bridge with Glu235 before binding dicarboxylic substrates (L-Glu or *α*-KG),[53] as shown in the crystal structures of native *h*OAT (Figure S11A) and inactivated *h*OAT (Figure S11B/C). Disruption of Arg-Glu salt bridges in aminotransferases was observed previously when the final adduct formed a H-bond with another arginine residue[29, 36] or when there was full occupation of the active site by a bulky adduct (Figure S11D)[47]. In the case of *h*OAT-**14** the Arg413-Glu235 salt bridge is disrupted and interactions of Arg413 with both Gln266 and Glu235 can be observed. One of the oxygens in the carboxylate group of Glu235 is 3.6 Å away from the amido group of the Gln266 side chain and potentially could also form a hydrogen bond with this residue. However, neither Arg413 nor Glu235 forms a H-bond with the adduct, and the space proximal to these residues remains unoccupied, indicating that this stable salt bridge might be broken during the inactivation process.

Molecular Docking and Molecular Dynamics (MD) Simulations

Although the structure of the final adduct for *h*OAT-**14** is well supported by mass spectrometry and crystallography studies, the inactivation process is not quite clear. Two covalent bonds are formed with catalytic Lys292 and *Thr322 from the other chain, which potentially resulted from two nucleophilic attacks at the Michael acceptor intermediate (Scheme 4), but it cannot be concluded which covalent bond formed first. Catalytic Lys292 is more nucleophilic than *Thr322, which was found to react with active intermediates previously. However, the highly electrophilic difluoro Michael acceptor was previously found to react with water molecules in the active site of the aminotransferase (Scheme 2),[29, 36] supporting its potential to react initially with *Thr322. The cocrystal structure of *h*OAT inactivated by **14** (Figure 4) provides some clues for further elucidation of the inactivation process. Imine isomerization appears to occur between proposed intermediate **27** and final adduct **32`**, which might happen after the nucleophilic attacks by the two residues or result from rotation/tautomerization of adduct **32**. It seems highly unlikely that after attachment of two residues a 180° bond rotation would occur readily. However, rotation prior to nucleophilic attack might be possible, transforming **46** to **47**, then on to **27’**, possibly resulting from steric hindrance between the fluorine of the warhead and the internal H-bond (Scheme S2). The salt-bridge between Arg413 and Glu235 becomes disrupted, as shown in the cocrystal structure (Figure 4), which might play an important role during the rotation and inactivation process. To evaluate the potential and sequence of the nucleophilic addition steps (Lys292 *vs.* *Thr322), molecular docking and molecular dynamics (MD) simulations of intermediates were conducted in the active site of *h*OAT, with salt bridge maintained and disrupted, respectively.

Intermediate **25** showed similar docking poses in the active site of *h*OAT with the salt bridge maintained (Figure S12A) and disrupted (Figure S12B), in which the **γ**-proton is positioned close to catalytic residue Lys292, facilitating the following deprotonation step. In addition, the salt bridge status demonstrated a significant effect on the docking poses of intermediates **27** and **27`**. For the case of the salt bridge maintained, the carboxylate of intermediate **27** establishes hydrogen bonds with Tyr55, and the warhead is located close to Lys292, Arg413, and Glu235 (Figure S12C). No significant change was observed after a 25 ns MD simulation (Figure 5A), in which the C_F is slightly closer to Lys292 (5.8 ±

0.4 Å) than to *Thr322 (7.0 ± 0.8 Å), with an average difference of 1.2 Å (Figure 5A). Considering the higher nucleophilicity of the amino group, Lys292 is expected to react with the warhead preferentially if this binding pose were presented (Figure 5A). Furthermore, rotamer intermediate **27`** would not fit well if the salt bridge were maintained, in which case the PLP moiety would slip away from its original position.

For the case where the salt bridge of *h*OAT is disrupted, there is a strong interaction between Arg413 and the carboxylate of intermediate **27** in the docking studies, which forces the warhead to rotate to the other side near Tyr55 and *Thr322 (Figure S12D). However, the MD simulation showed that it failed to maintain these interactions, and the warhead group stayed away from both Lys292 (7.4 ± 0.3 Å) and *Thr322 (7.3 ± 0.7 Å), indicating that inactivation could not be achieved with this binding pose (Figure 5B). However, molecular docking results of rotamer intermediate **27`** showed that its carboxylate formed similar interactions with Arg413 with its internal H-bond maintained in the active site of *h*OAT when the salt bridge was disrupted (Figure S12E). MD simulations confirmed a stable interaction between **27`** and surrounding residues, maintaining its warhead moiety positioned much closer to *Thr322 (3.4 ± 0.3 Å) than to Lys292 (5.9 ± 0.4 Å), which would favor a reaction with the threonine residue (Figure 5C). Notably, Lys292 is positoned near *Thr322 with an average distance of 3.4 ± 0.5 Å (Figure 5C), which is similar to that seen in the cocrystal structure of *h*OAT with tight-binding adducts (Figures S11B & S11C). Thus, we hypothesize that final adduct **32`** could be generated from either intermediate **36** or **49**, depending upon the order of nucleophilic additions (Scheme S2).

Soaking structure of *h*OAT inactivated by 14

As indicated in the above molecular docking and MD simulation studies, the order of nucleophilic addition by the two residues could be determined by different binding poses of **27** (Figure 5A, Figure S12C) and **27`** (Figure 5C, Figure S12E), whose carboxylate interacts with either Tyr55 or Arg413 on the basis of the status of the Arg413/Glu235 salt bridge. Previously, we successfully obtained the active intermediate for *h*OAT inactivated by **10** via soaking experiments.[60] To determine the dominant binding orientation, soaking experiments of *h*OAT with **14** were performed. Holoenzyme *h*OAT crystals were obtained within four days and then soaked with 5 mM **14** (1 μL added to a 4 μL hanging drop) for different time durations from 17 to 44 minutes. After soaking, the crystals were transferred to a cryo-protectant solution and flash-frozen in liquid nitrogen. The crystal soaked for 44 minutes diffracted to a resolution of 2.1 Å, and its structure was solved using molecular replacement and then compared to the *h*OAT-**14.** cocrystal structure.

Satisfyingly, intermediate **36** (Scheme S2) was trapped in the soaking study of *h*OAT and **14** (Figure 6) based on observed electron density, as found in one out of three copies in an asymmetric unit, in which the connection between the warhead and *Thr322 was confirmed prior to the attachment of Lys292. In the other two protein copies, relatively weak electron density was observed between the warhead and both Lys292 and *Thr322 (Figure S13), suggesting some proportion of Lys292 had already begun to react with the warhead of **36**. Importantly, the Arg413-Glu235 salt bridge was disrupted, and the “free” arginine residue established a stable H-bond with the carboxylate of **36**, which could explain the broken salt bridge in the cocrystal structure of *h*OAT inactivated by **14** (Figure 4). Overall, the soaking structure is quite similar to the docking pose of active intermediate **27`** (Figure S12E), whose warhead is positioned close to *Thr322 with an internal H-bond maintained. Supported by the above experiments, adduct **36** is proposed to be formed by the initial nucleophilic attack of *Thr322 on the difluoromethylenyl group of intermediate **27`**, followed by reaction of **36** with Lys292 to afford final adduct **32`** (Scheme S2). This outcome suggests that the inactivation mechanistic pathway follows from rotation of **46** to **47** prior to nucleophilic attack by either active site residue.

Turnover Mechanism

MBIs act as substrates that bind at the active sites of target enzymes initially; therefore, it is common that many MBIs are converted to metabolites during the inactivation process.[25] On the basis of the reported turnover mechanisms for **1** and **5** with GABA-AT, [33, 36] two possible turnover pathways for **14** by *h*OAT are proposed, with the release of PMP or PLP, respectively (Scheme 5). Lys292-assisted deprotonation of Schiff base **25** affords intermediate **26**, followed by the protonation at different positions to give intermediate **27`** (*pathway a*) or **33** (*pathway b*). Intermediate **27`** could be further hydrolyzed with the release of PMP and metabolite **37** (*pathway a1*) or **38** (*pathway a2*), which is similar to the transamination of ornithine by *h*OAT (Scheme 1). The reaction of intermediate **33** with Lys292 could afford intermediate **39**, followed by the release of PLP and metabolite **40** (*pathway b1*) or **42** (*pathway b2*) with hydrolysis to **44**. Enamine **40** could be hydrolyzed to give ketone **41**; imine **42** could undergo aromatization to generate metabolite **43**, and aromatization of **44** would give **45**. To identify which of the above-mentioned turnover pathways are involved, partition ratio and fluoride ion release experiments and mass spectrometric analysis of metabolites were carried out.

Partition Ratio and Fluoride Ion Release

The partition ratio is used to determine the ratio of degradation to inactivation, calculated by titrating the enzyme with varying equivalents of inactivator. Ideally, a linear relationship (between enzyme activity remaining and equivalents of compound incubated) can be extrapolated to yield the exact equivalents (the intercept with the x-axis, turnover number) required to inactivate the enzyme completely. Since this number includes the one molecule of inactivator required to inactivate one enzyme monomer, the partition ratio is equal to the turnover number minus one. Therefore, the partition ratio of **14** (0.6) was determined by titrating *h*OAT with varying equivalents of inactivators (Figure S14).

Different equivalents of fluoride ions can be released in PLP and PMP turnover pathways. If PMP is formed in the turnover mechanism, it cannot be converted back to PLP in the absence of α-KG, which results in, at most, two equivalents of fluoride ions released (*pathway a*, Scheme 5); more equivalents of fluoride ion would be released in the presence of α-KG if PMP is formed after the fluoride ion release step (*pathway a1*, Scheme 5). If PLP is regenerated during the turnover mechanism, at least two equivalents of fluoride ion will be released in the absence of α-KG (*pathway b*, Scheme 5 in addition to the fluoride ion released for inactivation), which should be close to the equivalents in the presence of α-KG. On the basis of the partition ratio and the confirmed inactivation mechanism for **14**, the theoretical equivalents of fluoride ions that are released per enzyme active site during different turnover pathways can be calculated in the presence and absence of α-KG (Table 3). The concentration of released fluoride ions can be monitored by a fluoride ion-selective electrode. When *h*OAT was inactivated with an excess of **14**, 2.9 equivalents of fluoride ions were released in the presence of α-KG and 2.7 equivalents of fluoride ions were released in the absence of α-KG (Table 3). These results indicate that the regeneration of PLP is involved in the turnover mechanism for **14**, in which the experimental fluoride ions released are close to the theoretical calculations for turnover *pathway b2* (Scheme 5).

Mass Spectrometry-Based Analysis of Turnover Products

To identify the potential metabolites generated during the inactivation process of *h*OAT by **14**, the inactivated *h*OAT sample was filtered through a 10 kDa MWCO filter, followed by the use of untargeted LC-HRMS with alternating +/− mode electrospray to analyze the filtrate obtained. Among the possible metabolites proposed in Scheme 5, only metabolite **43** (observed: 170.0610 *m/z*, $[M+H]^+$; theoretical: 170.0612 *m/z*) in *pathway b2* was detected, followed by the confirmation of its fragmentation spectrum (Figure 7). Notably, metabolite **45** in *pathway b2* was not observed by HRMS, indicating the aromatization step is much faster than the hydrolysis step. Precursor **42** was generated in the active site that is not filled with “free” water molecules. Thus, we believe **42** probably has been converted to amine **43** before being transported out of the pocket, which prevented further hydrolysis. Taken together, both the metabolomic result and the fluoride ion release experiments indicate that **14** undergoes turnover by *pathway b2* with the regeneration of PLP and the release of metabolite **43** (Scheme 5).

Plausible Mechanism for 14 with *h*OAT

On the basis of the above inactivation and turnover mechanism studies, a modified pathway for **14** with *h*OAT is proposed in Scheme 6. Initially, Schiff base **25** was generated from **14** and PLP, followed by deprotonation at the γ-position. According to the partition ratio (0.6) of **14** (Figure S14), 63% of **26** is converted to active intermediate **27`** (pathway a), which involves rotation about the C-N single bond of **46** and protonation at the PLP-C4` position of **48**. Molecular docking and MD simulation studies suggest that the carboxylate of **27`** forms a stable interaction with Arg413 (Figure 5C) when the original salt bridge is disrupted. This binding pose allows the warhead to be positioned close to *Thr322 from the other chain (Figure 5C, 3.4 Å vs. 5.9 Å), leading to the formation of **36**, which was trapped in the soaking crystal structure (Figure 6). Considering the short distance (3.4 Å) between Lys292 and *Thr322 observed in the MD simulation studies of **27`**, Lys292 might play a role in activating *Thr322 for this nucleophilic attack, which is similar to the activation of water molecules by Lys329 in the case of **5** and **9** with GABA-AT (Scheme 2). The covalent attachment to *Thr322 pulls the warhead closer to Lys292 and allows a second nucleophilic attack on **36** to give **50**. Finally, adduct **32`** is formed to release the potential strain from two covalent attachments (Figure 4), while its carboxylate stays away from Arg413 and forms a H-bond with Tyr55 instead. Interestingly, Arg413 and Glu235 do not form a salt bridge after inactivation but interact with nearby Gln266 (Figure 4). The formation of the double-covalent adduct (**32`**) in the active site of *h*OAT-**14** is supported by three types of protein MS and X-ray crystallography. With regard to the turnover pathway, 37% of intermediate **26** is converted to intermediate **33** by protonation at the difluoromethylenyl group, followed by Lys292 attack at the PLP iminium group, leading to regeneration of PLP and the release of **43** as the final metabolite. Among the proposed metabolites (Scheme 5), only **43** was detected by HRMS and confirmed by its fragmentation spectrum (Figure 7) and results of fluoride ion release experiments (Table 3).

CONCLUSIONS

Recently, selective pharmacological inhibition of human ornithine aminotransferase (*h*OAT) has been shown as a potential therapeutic approach to treat hepatocellular carcinoma (HCC) and other related cancers. Inspired by the inactivation mechanism for aminotransferase inactivators **5** and **9**, a novel series of six-membered ring analogs (**12-15**) was rationally designed and chirally synthesized on the basis of the difference in the active sites of aminotransferases. Among them, analog **14** was identified as a selective *h*OAT inactivator and is 22 times more potent than analog **10**, which has good *in vivo* anticancer activity. A plausible mechanism for **14** with *h*OAT is proposed (Scheme 6) on the basis of four distinct applications of mass spectrometry, two types of protein crystallography, and molecular dynamics (MD) simulations with the aid of a dialysis experiment, total turnover, and measurement of fluoride ion release. Notably, this is the first time in which native mass spectrometry and top-down proteomics have been applied to a mechanistic study of a PLP-dependent enzyme inactivator. Remarkably, double-covalent adduct **32`** was formed in the active site of *h*OAT via sequential nucleophilic attacks, first by the noncatalytic residue *Thr322 and then by the catalytic residue Lys292, at the warhead of active intermediate **27`**. To the best of our knowledge, this is the first example of an MBI forming a single adduct with two covalent bonds from two residues in the active site of an enzyme, one of which a noncatalytic residue. Moreover, an unusual turnover mechanism also has been demonstrated, in which aromatic metabolite **43** was generated along with regeneration of cofactor PLP. Interestingly, no water molecule was involved in the inactivation mechanism of *h*OAT with **14,** whereas water molecules play an important role in the mechanisms of **5** and **9** with GABA-AT (Scheme 2). We believe this mechanistic difference derives from the enzymatic machinery of these two aminotransferases, which should contribute to the further rational design of selective inactivators.

Supplementary Material

Refer to Web version on PubMed Central for supplementary material.

ACKNOWLEDGMENTS

We are grateful to the National Institutes of Health (grant R01 DA030604 to R.B.S. and grants P30 DA018310 and S10OD025194 to N.L.K.) for financial support. This work used the Extreme Science and Engineering Discovery Environment (XSEDE) Comet Bridges Stampede2 through allocation TG-CHE190070, which is supported by National Science Foundation grant number ACI-1548562. This work made use of the IMSERC at Northwestern University, which has received support from the Soft and Hybrid Nanotechnology Experimental (SHyNE) Resource (NSF NNCI-1542205), the State of Illinois, and the International Institute for Nanotechnology (IIN). X-ray diffraction data collection used resources of the Advanced Photon Source, a U.S. Department of Energy (DOE) Office of Science User Facility operated for the DOE Office of Science by Argonne National Laboratory under contract no. DE- AC02-06CH11357. The use of LS-CAT Sector 21 was supported by the Michigan Economic

Development Corporation and the Michigan Technology Tri-Corridor (grant 085P1000817). We thank Dr. Joseph Brunzelle at LS-CAT for help on data collection. We thank Dr. Matthew J. Moschitto and Dr. Sida Shen for constructive comments and Dr. Mauricio T. Tavares and Dr. Glaucio M. Ferreira for help on MD simulation studies.

ABBREVIATIONS

DMP	Dess-Martin periodinane
PMB	*p*-methoxybenzyl
CAN	cerium (IV) ammonium nitrate
Boc	*tert*-butyloxycarbonyl
KHMDS	potassium bis(trimethylsilyl)amide
DIPEA	*N*,*N*-diisopropylethylamine
Boc_2O	di-*tert*-butyldicarbonate
***m*-CPBA**	meta-chloroperoxybenzoic acid
^{t}BuOK	potassium *tert*-butoxide
DMAP	4-dimethylaminopyridine
DMF	dimethylformamide
DCM	dichloromethane

REFERENCES

1. Sayiner M; Golabi P; Younossi ZMDisease burden of hepatocellular carcinoma: a global perspective. Digest Dis. Sci2019, 64, 910–917. [PubMed: 30835028]
2. Personeni N; Rimassa L. Hepatocellular carcinoma: a global disease in need of individualized treatment strategies. J. Oncol. Pract2017, 13, 368–370. [PubMed: 28605613]
3. Sherman M; Bruix J; Porayko M; Tran T; Comm APGScreening for hepatocellular carcinoma: The rationale for the American association for the study of liver diseases recommendations. Hepatology2012, 56, 793–796. [PubMed: 22689409]
4. Yang JD; Roberts LRHepatocellular carcinoma: a global view. Nat. Rev. Gastro. Hepat2010, 7, 448–458.
5. Leathers JS; Balderramo D; Prieto J; Diehl F; Gonzalez-Ballerga E; Ferreiro MR; Carrera E; Barreyro F; Diaz-Ferrer J; Singh D; Mattos AZ; Carrilho F; Debes JDSorafenib for treatment of hepatocellular carcinoma a survival analysis from the aouth american liver research network. J. Clin. Gastroenterol2019, 53, 464–469. [PubMed: 29952857]
6. de Rosamel L; Blanc JFEmerging tyrosine kinase inhibitors for the treatment of hepatocellular carcinoma. Expert Opin. Emerg. Dr2017, 22, 175–190.
7. Milgrom DP; Maluccio MA; Koniaris LGManagement of hepatocellular carcinoma (HCC). Curr. Surg. Rep2016, 4, 20; DOI 10.1007/s40137-016-0143-4.
8. de Lope CR; Tremosini S; Forner A; Reig M; Bruix J. Management of HCC. J. Hepatol2012, 56, S75–S87. [PubMed: 22300468]
9. Ginguay A; Cynober L; Curis E; Nicolis I. Ornithine aminotransferase, an important glutamate-metabolizing enzyme at the crossroads of multiple metabolic pathways. Biology (Basel)2017, 6 (1), 18; doi:10.3390/biology6010018.

10. Zigmond E; Ben Ya'acov A; Lee H; Lichtenstein Y; Shalev Z; Smith Y; Zolotarov L; Ziv E; Kalman R; Le HV; Lu HJ; Silverman RB; Ilant Y. Suppression of hepatocellular carcinoma by inhibition of overexpressed ornithine aminotransferase. ACS Med. Chem. Lett2015, 6, 840–844. [PubMed: 26288681]
11. John RAPyridoxal Phosphate-Dependent Enzymes. Biochim. Biophys. Acta1995, 1248, 81–96.. [PubMed: 7748903]
12. Herzfeld A; Knox WEThe properties developmental formation and estrogen induction of ornithine aminotransferase in rat tissues. J. Biol. Chem1968, 243, 3327–3332. [PubMed: 4298129]
13. Peraino C; Bunville LG; Tahmisia TNChemical physical and morphological properties of ornithine aminotransferase from rat liver. J. Biol. Chem1969, 244, 2241–2249. [PubMed: 5783831]
14. Ding Z; Ericksen RE; Escande-Beillard N; Lee QY; Loh A; Denil S; Steckel M; Haegebarth A; Wai Ho TS; Chow P; Toh HC; Reversade B; Gruenewald S; Han W. Metabolic pathway analyses identify proline biosynthesis pathway as a promoter of liver tumorigenesis. J. Hepatol2020, 72, 725–735. [PubMed: 31726117]
15. Altman BJ; Stine ZE; Dang CVFrom Krebs to clinic: glutamine metabolism to cancer therapy. Nat. Rev. Cancer2016, 16, 619–634. [PubMed: 27492215]
16. Phang JM; Liu W; Hancock CN; Fischer JWProline metabolism and cancer: emerging links to glutamine and collagen. Curr. Opin. Clin. Nutr. Metab. Care2015, 18, 71–77. [PubMed: 25474014]
17. Phang JM; Liu W; Zabirnyk O. Proline metabolism and microenvironmental stress. Annu. Rev. Nutr2010, 30, 441–463. [PubMed: 20415579]
18. Tang L; Zeng J; Geng P; Fang C; Wang Y; Sun M; Wang C; Wang J; Yin P; Hu C; Guo L; Yu J; Gao P; Li E; Zhuang Z; Xu G; Liu Y. Global metabolic profiling identifies a pivotal role of proline and hydroxyproline metabolism in supporting hypoxic response in hepatocellular varcinoma. Clin. Cancer Res2018, 24, 474–485. [PubMed: 29084919]
19. Cadoret A; Ovejero C; Terris B; Souil E; Levy L; Lamers WH; Kitajewski J; Kahn A; Perret C. New targets of beta-catenin signaling in the liver are involved in the glutamine metabolism. Oncogene2002, 21, 8293–8301. [PubMed: 12447692]
20. Colnot S; Decaens T; Niwa-Kawakita M; Godard C; Hamard G; Kahn A; Giovannini M; Perret C. Liver-targeted disruption of Apc in mice activates beta-catenin signaling and leads to hepatocellular carcinomas. P. Natl. Acad. Sci. USA2004, 101, 17216–17221.
21. Liu YF; Wu L; Li K; Liu FR; Wang L; Zhang DL; Zhou J; Ma X; Wang SY; Yang SYOrnithine aminotransferase promoted the proliferation and metastasis of non-small cell lung cancer via upregulation of miR-21. J. Cell Physiol2019, 234, 12828–12838. [PubMed: 30549035]
22. Markova M; Peneff C; Hewlins MJE; Schirmer T; John RADeterminants of substrate specificity in omega-aminotransferases. J. Biol. Chem2005, 280, 36409–36416. [PubMed: 16096275]
23. Mehta PK; Hale TI; Christen P. Evolutionary relationships among aminotransferases - tyrosine aminotransferase, histidinol-phosphate aminotransferase, and aspartate-aminotransferase are homologous proteins. Eur. J. Biochem1989, 186, 249–253. [PubMed: 2574669]
24. Cooper AJLGlutamate-gamma-aminobutyrate transaminase. Methods Enzymol. 1985, 113, 80–82. [PubMed: 3911014]
25. Silverman RBDesign and mechanism of GABA aminotransferase inactivators. treatments for epilepsies and addictions. Chem. Rev2018, 118, 4037–4070. [PubMed: 29569907]
26. Silverman RBMechanism-based enzyme inactivators. Methods Enzymol. 1995, 249, 240–283. [PubMed: 7791614]
27. Rando RRMechanism-based enzyme inactivators. Pharmacol. Rev1984, 36, 111–142. [PubMed: 6379680]
28. Walsh CTSuicide Substrates, mechanism based enzyme inactivators - recent developments. Annu. Rev. Biochem1984, 53, 493–535. [PubMed: 6433782]
29. Juncosa JI; Takaya K; Le HV; Moschitto MJ; Weerawarna PM; Mascarenhas R; Liu DL; Dewey SL; Silverman RBDesign and mechanism of (S)-3-amino-4-(difluoromethylenyl)cyclopent-1-ene-1-carboxylic acid, a highly potent gamma-aminobutyric acid aminotransferase inactivator for the treatment of addiction. J. Am. Chem. Soc2018, 140, 2151–2164. [PubMed: 29381352]
30. Pan Y; Gerasimov MR; Kvist T; Wellendorph P; Madsen KK; Pera E; Lee H; Schousboe A; Chebib M; Brauner-Osborne H; Craft CM; Brodie JD; Schiffer WK; Dewey SL; Miller SR;

Silverman RB(1S, 3S)-3-Amino-4-difluoromethylenyl-1-cyclopentanoic acid (CPP-115), a potent gamma-aminobutyric acid aminotransferase inactivator for the treatment of cocaine addiction. J. Med. Chem2012, 55, 357–366. [PubMed: 22128851]

31. Sivenius MR; Ylinen A; Murros K; Matilainen R; Riekkinen P. Double-blind dose reduction study of vigabatrin in complex partial epilepsy. Epilepsia1987, 28, 688–92. [PubMed: 3319536]
32. Wheless JW; Ramsay RE; Collins SDVigabatrin. Neurotherapeutics2007, 4, 163–172. [PubMed: 17199033]
33. Nanavati SM; Silverman RBMechanisms of inactivation of gamma-aminobutyric-acid aminotransferase by the antiepilepsy drug gamma-vinyl GABA (vigabatrin). J. Am. Chem. Soc1991, 113, 9341–9349.
34. Silverman RBThe 2011 E. B. Hershberg Award for Important Discoveries in Medicinally Active Substances: (1S,3S)-3-Amino-4-difluoromethylenyl-1-cyclopentanoic acid (CPP-115), a GABA Aminotransferase Inactivator and New Treatment for Drug Addiction and Infantile Spasms. J. Med. Chem2012, 55, 567–575. [PubMed: 22168767]
35. Pan Y; Qiu J; Silverman RBDesign, synthesis, and biological activity of a difluoro-substituted, conformationally rigid vigabatrin analogue as a potent gamma-aminobutyric acid aminotransferase inhibitor. J. Med. Chem2003, 46, 5292–5293. [PubMed: 14640537]
36. Lee H; Doud EH; Wu R; Sanishvili R; Juncosa JI; Liu DL; Kelleher NL; Silverman RBMechanism of inactivation of gamma-aminobutyric acid aminotransferase by (1S,3S)-3-amino-4-difluoromethylene-1-cyclopentanoic acid (CPP-115). J. Am. Chem. Soc2015, 137, 2628–2640. [PubMed: 25616005]
37. Briggs SW; Mowrey W; Hall CB; Galanopoulou ASCPP-115, a vigabatrin analogue, decreases spasms in the multiple-hit rat model of infantile spasms. Epilepsia2014, 55, 94–102. [PubMed: 24321005]
38. Doumlele K; Conway E; Hedlund J; Tolete P; Devinsky O, A case report on the efficacy of vigabatrin analogue (1S, 3S)-3-amino-4-difluoromethylenyl-1-cyclopentanoic acid (CPP-115) in a patient with infantile spasms. Epilepsy Behav. Case2016, 6, 67–69.
39. Lee H; Juncosa JI; Silverman RBOrnithine aminotransferase versus GABA aminotransferase: implications for the design of new anticancer drugs. Med. Res. Rev2015, 35, 286–305. [PubMed: 25145640]
40. Zhu W; Doubleday PF; Catlin DS; Weerawarna PM; Butrin A; Shen S; Wawrzak Z; Kelleher NL; Liu D; Silverman RBA remarkable difference that one fluorine atom confers on the mechanisms of inactivation of human ornithine aminotransferase by two cyclohexene analogues of gamma-aminobutyric acid. J. Am. Chem. Soc2020, 142, 4892–4903. [PubMed: 32114761]
41. Yeung YY; Hong S; Corey EJA short enantioselective pathway for the synthesis of the anti-influenza neuramidase inhibitor oseltamivir from 1,3-butadiene and acrylic acid. J. Am. Chem. Soc2006, 128, 6310–6311. [PubMed: 16683783]
42. Moschitto MJ; Silverman RBSynthesis of (S)-3-amino-4-(difluorornethylenyl)-cyclopent-1-ene-1-carboxylic acid (OV329), a potent inactivator of gamma-aminobutyric acid aminotransferase. Org. Lett2018, 20, 4589–4592. [PubMed: 30009604]
43. Rando RRMechanism of irreversible inhibition of gamma-aminobutyric acid-alpha-ketoglutaric acid transaminase by neurotoxin gabaculine. Biochemistry1977, 16, 4604–4610. [PubMed: 410442]
44. Shah SA; Shen BW; Brunger ATHuman ornithine aminotransferase complexed with L-canaline and gabaculine: structural basis for substrate recognition. Structure1997, 5, 1067–1075. [PubMed: 9309222]
45. Kobayashi K; Miyazawa S; Endo A. Isolation and inhibitory activity of gabaculine, a new potent inhibitor of gamma-aminobutyrate aminotransferase produced by a streptomyces. Febs. Lett1977, 76, 207–210. [PubMed: 862902]
46. Skinner OS; Haverland NA; Fornelli L; Melani RD; Do Vale LHF; Seckler HS; Doubleday PF; Schachner LF; Srzentic K; Kelleher NL; Compton PDTop-down characterization of endogenous protein complexes with native proteomics. Nat. Chem. Biol2018, 14, 36–41. [PubMed: 29131144]
47. Moschitto MJ; Doubleday PF; Catlin DS; Kelleher NL; Liu DL; Silverman RBMechanism of inactivation of ornithine aminotransferase by (1S,3S)-3-amino-4-(hexafluoropropan-2-

ylidenyl)cyclopentane-1-carboxylic Acid. J. Am. Chem. Soc2019, 141, 10711–10721. [PubMed: 31251613]

48. Shen SD; Doubleday PF; Weerawarna PM; Zhu W; Kelleher NL; Silverman RBMechanism-Based Design of 3-Amino-4-Halocyclopentenecarboxylic Acids as Inactivators of GABA Aminotransferase. ACS Med. Chem. Lett2020, 11, 1949–1955. [PubMed: 33062178]
49. Zubarev RA; Horn DM; Fridriksson EK; Kelleher NL; Kruger NA; Lewis MA; Carpenter BK; McLafferty FWElectron capture dissociation for structural characterization of multiply charged protein cations. Anal. Chem2000, 72, 563–573. [PubMed: 10695143]
50. Liu F; Lossl P; Scheltema R; Viner R; Heck AJROptimized fragmentation schemes and data analysis strategies for proteome-wide cross-link identification. Nat. Commun2017, 8, 15473. [PubMed: 28524877]
51. Olsen JV; Macek B; Lange O; Makarov A; Horning S; Mann M. Higher-energy C-trap dissociation for peptide modification analysis. Nat. Methods2007, 4, 709–12. [PubMed: 17721543]
52. DeHart CJ; Fellers RT; Fornelli L; Kelleher NL; Thomas PMBioinformatics analysis of top-down mass spectrometry data with ProSight Lite. Methods Mol. Biol2017, 1558, 381–394. [PubMed: 28150248]
53. Shen BW; Hennig M; Hohenester E; Jansonius JN; Schirmer T. Crystal structure of human recombinant ornithine aminotransferase. J .Mol. Biol1998, 277, 81–102. [PubMed: 9514741]
54. Mascarenhas R; Le HV; Clevenger KD; Lehrer HJ; Ringe D; Kelleher NL; Silverman RB; Liu D. Selective targeting by a mechanism-based inactivator against pyridoxal 5’-phosphate-dependent enzymes: mechanisms of inactivation and alternative turnover. Biochemistry2017, 56, 4951–4961. [PubMed: 28816437]
55. Storici P; Capitani G; Muller R; Schirmer T; Jansonius JNCrystal structure of human ornithine aminotransferase complexed with the highly specific and potent inhibitor 5-fluoromethylornithine. J. Mol. Biol1999, 285, 297–309. [PubMed: 9878407]
56. Layer RWThe chemistry of imines. Chem. Rev1963, 63, 489–510.
57. Johnson JE; Morales NM; Gorczyca AM; Dolliver DD; McAllister MAMechanisms of acid-catalyzed Z/E isomerization of imines. J. Org. Chem2001, 66, 7979–7985. [PubMed: 11722194]
58. Galvez J; Guirado A. A theoretical study of topomerization of imine systems: inversion, rotation or mixed mechanisms?J. Comput. Chem2010, 31, 520–31. [PubMed: 19548252]
59. Traven’ VF; Ivanov IV; Panov AV; Safronova OB; Chibisova TASolvent-induced E/Z(C=N)-isomerization of imines of some hydroxy-substituted formylcoumarins. Russ. Chem.Bull2008, 57, 1989–1995.
60. Butrin A; Beaupre BA; Kadamandla N; Zhao P; Shen S; Silverman RB; Moran GR; Liu D. Structural and kinetic analyses reveal the dual inhibition modes of ornithine aminotransferase by (1S,3S)-3-Amino-4-(hexafluoropropan-2-ylidenyl)-cyclopentane-1-carboxylic Acid (BCF3). ACS Chem. Biol2021, 16, 67–75. [PubMed: 33316155]

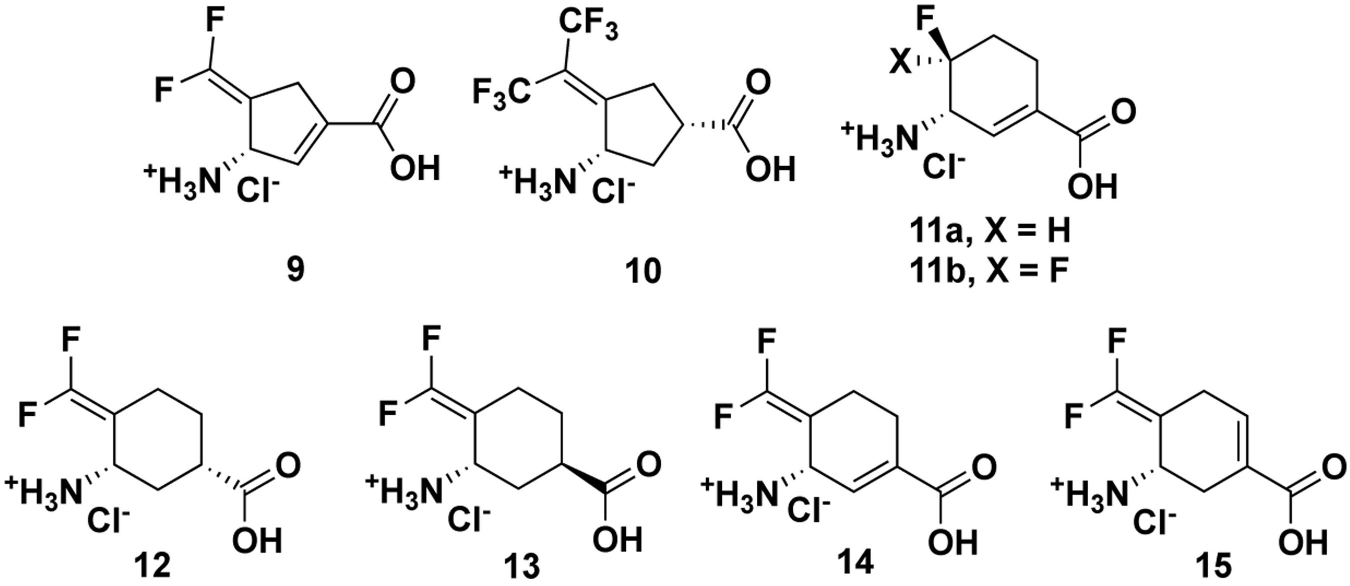

Figure 1.

Structures of analogs **9–15**

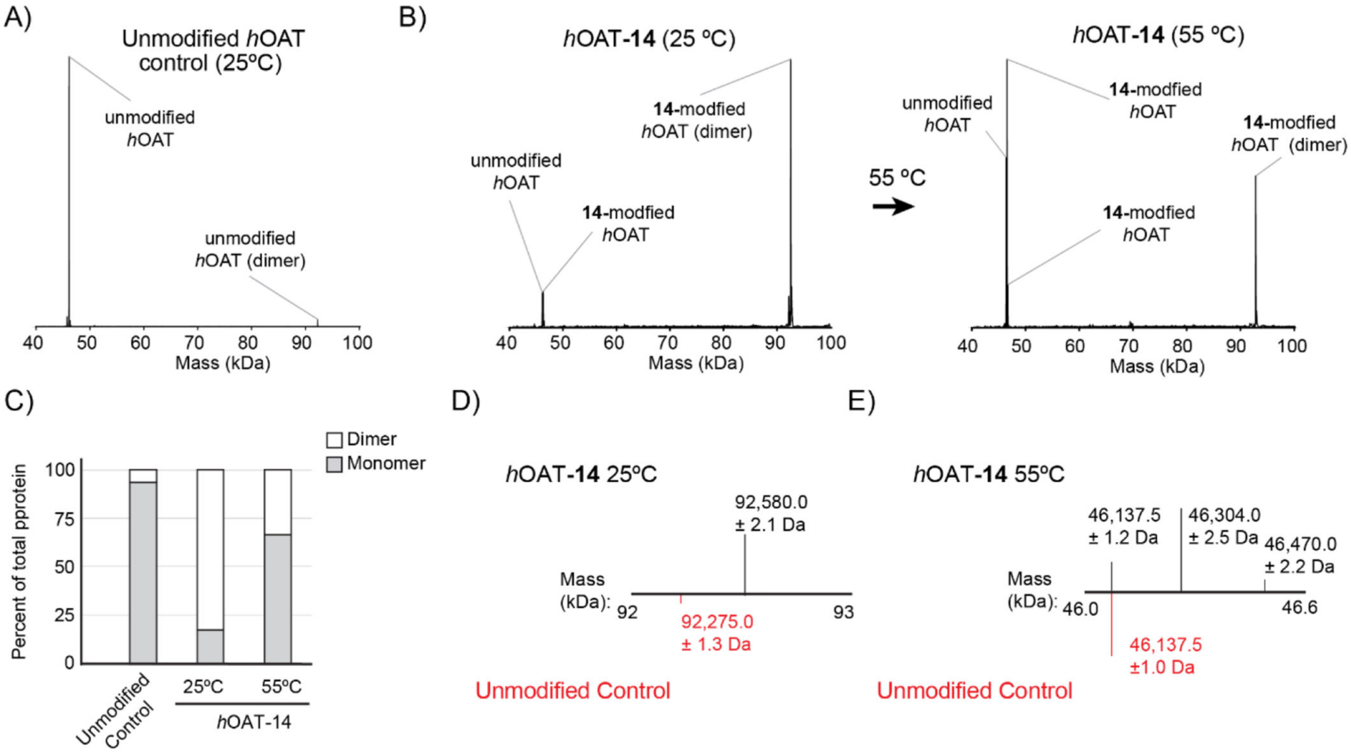

Figure 2.

Deconvoluted intact protein mass spectra for *h*OAT samples. (A) Unmodified *h*OAT. (B) *h*OAT-**14** analyzed at 25 °C (left); hOAT-**14** analyzed at 55 °C (right). (C) The ratio of monomer and dimer in samples as a percent of the total protein signal. (D) Expanded view of unmodified *h*OAT (red) and *h*OAT-**14** at 25 °C from 92–93 kDa. (E) Expanded view of unmodified *h*OAT (red) and *h*OAT-**14** at 55 °C from 46–46.6 kDa.

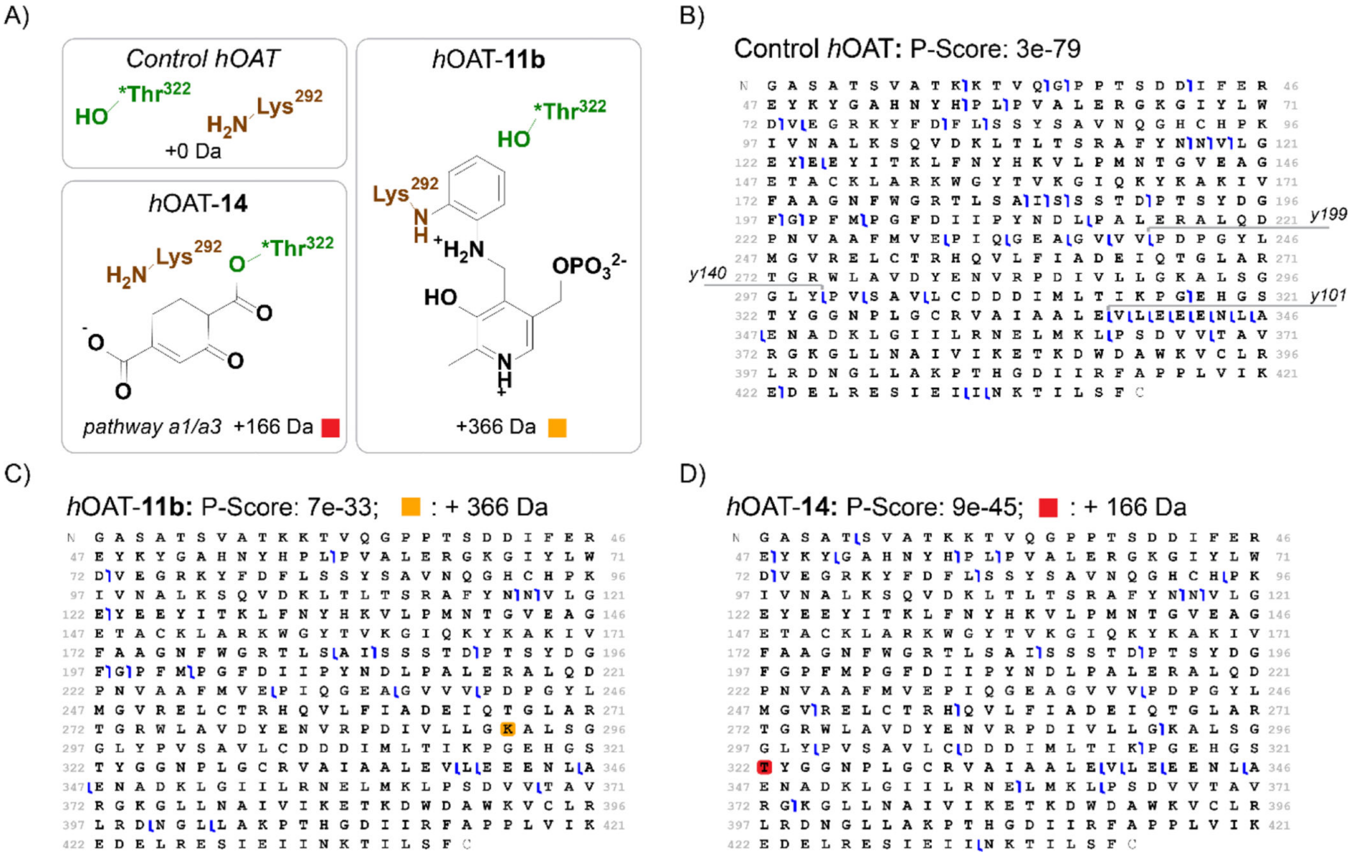

Figure 3.

Localization of covalent modifications on *h*OAT. (A) Proposed structures and masses corresponding to *h*OAT adducts. HCD fragmentation maps for (B) unmodified *h*OAT, (C) *h*OAT-**11b**, and (D) *h*OAT-**14**, with associated scoring metric[52] and modified residues colored for each adduct mass. Amino acid residues are numbered according to the full-length protein sequence (Uniprot accession: P04181) used in crystallography studies and not to the recombinantly expressed version of *h*OAT. For clarity, amino acid cleavage sites generating *y199*, *y140,* and *y101* are shown in panel (B).

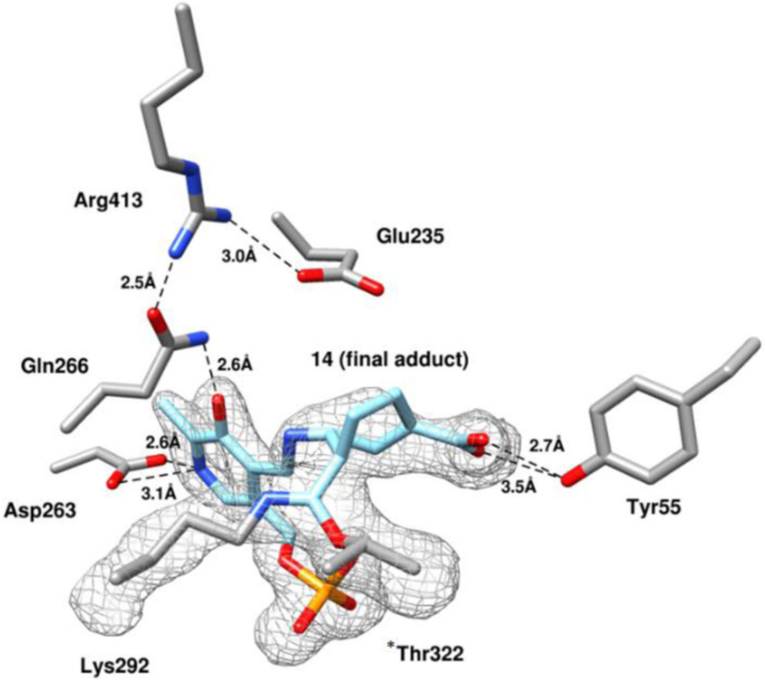

Figure 4.

Omit map (Fo-Fc at 2.5 σ) of the *h*OAT-**14** cocrystal structure. Black dashed lines indicate hydrogen bonds.

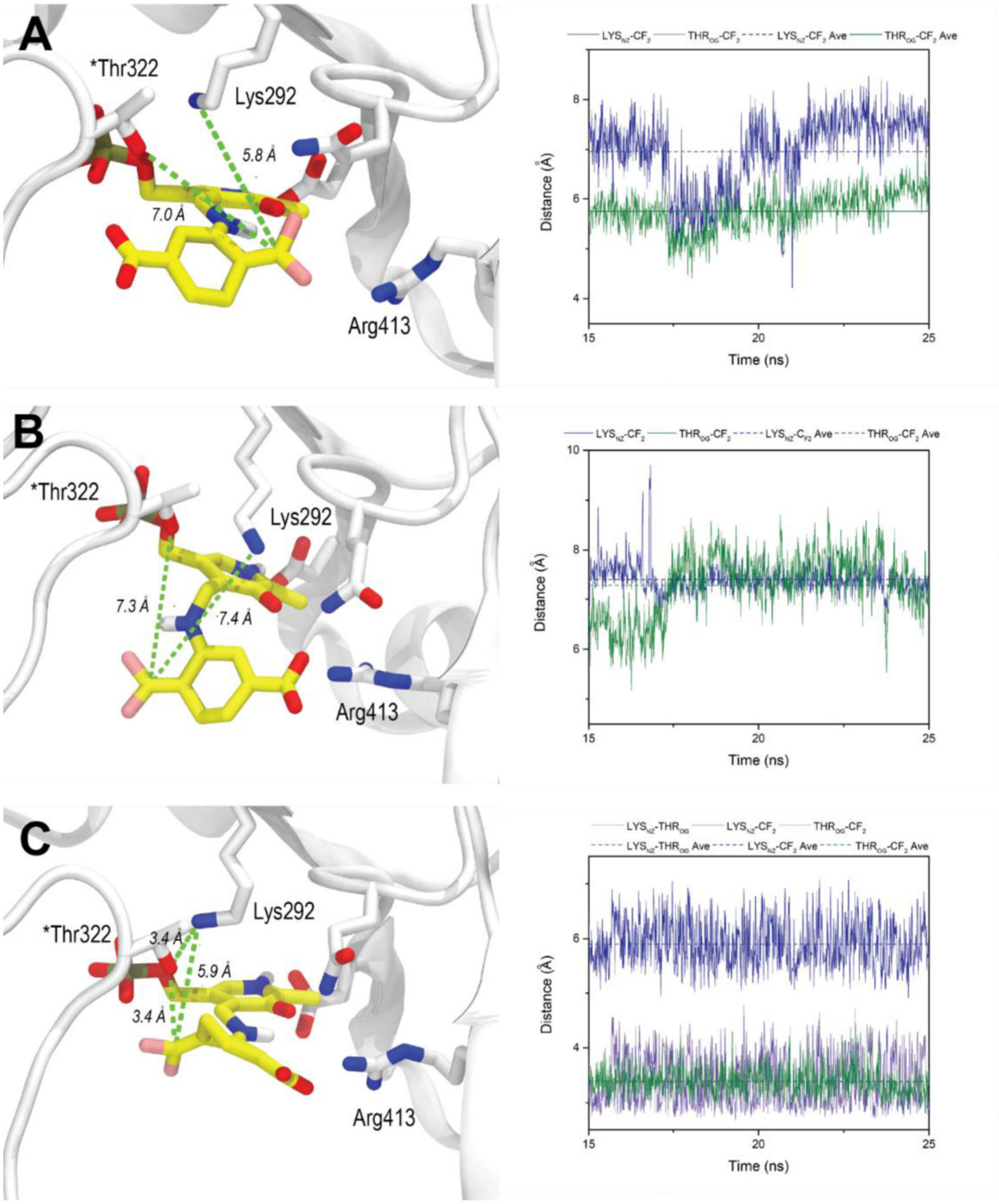

Figure 5.

Final binding poses and average distances for the nucleophilic additions for **27** and **27`** after 25 ns MD simulations. (A) MD simulation of **27** in the active site of *h*OAT with the intact salt bridge; (B) MD simulation of **27** in the active site of *h*OAT with the disrupted salt bridge; (C) MD simulation of **27`** in the active site of *h*OAT with the disrupted salt bridge.

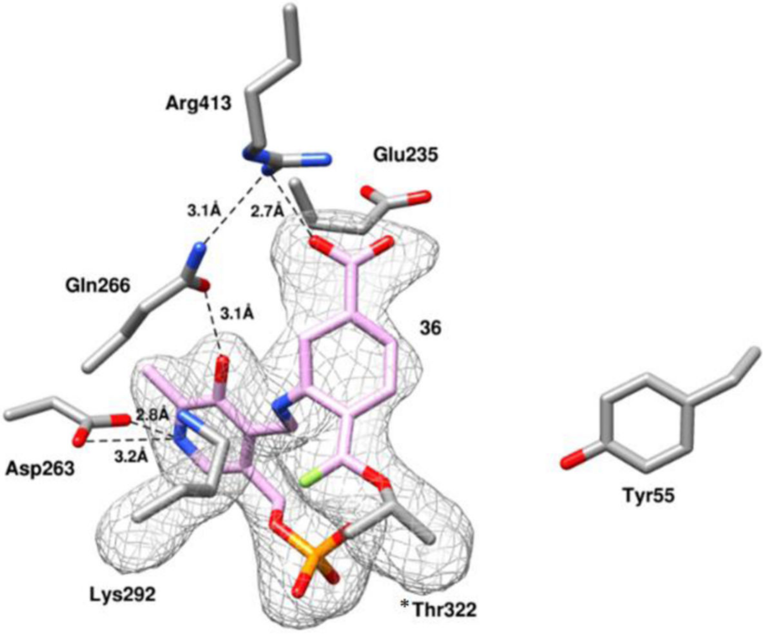

Figure 6.

Omit map (Fo-Fc at 2.5 σ) of intermediate **36** within the active site of *h*OAT. Black dashed lines indicate hydrogen bonds.

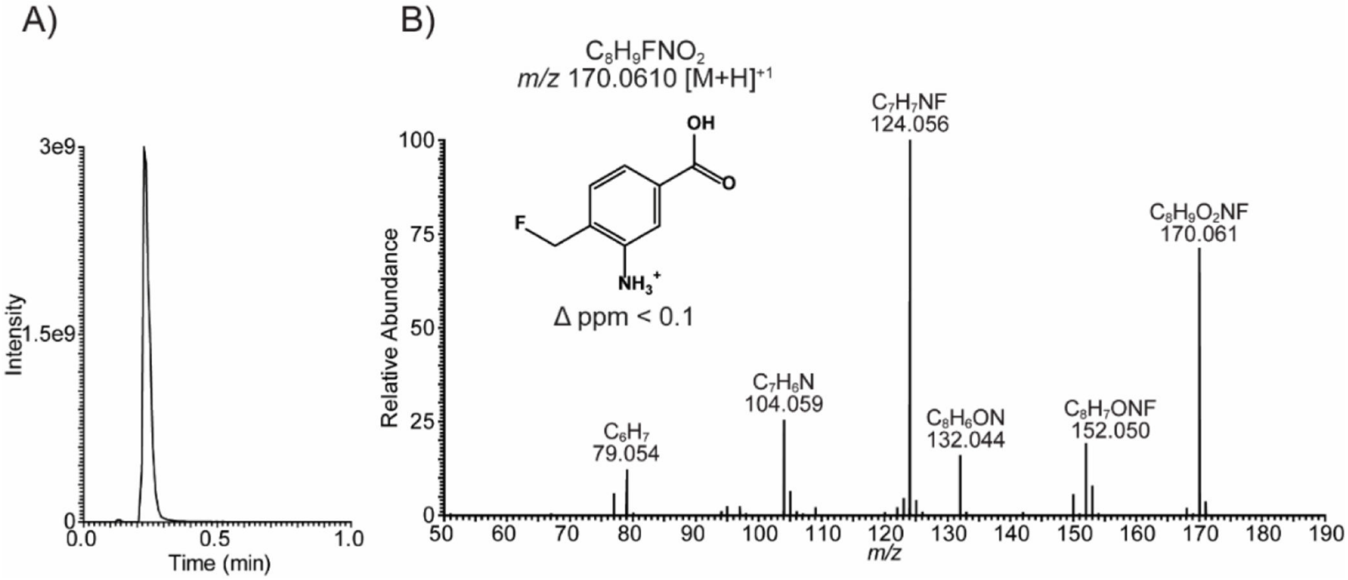

Figure 7.

Detection of metabolite **43** as the turnover product for *h*OAT-**14**. (A) Extracted ion chromatogram for **43** (+ESI, 170.04–170.08 *m/z*). (B) Confirmation of metabolite **43** using tandem mass spectrometry

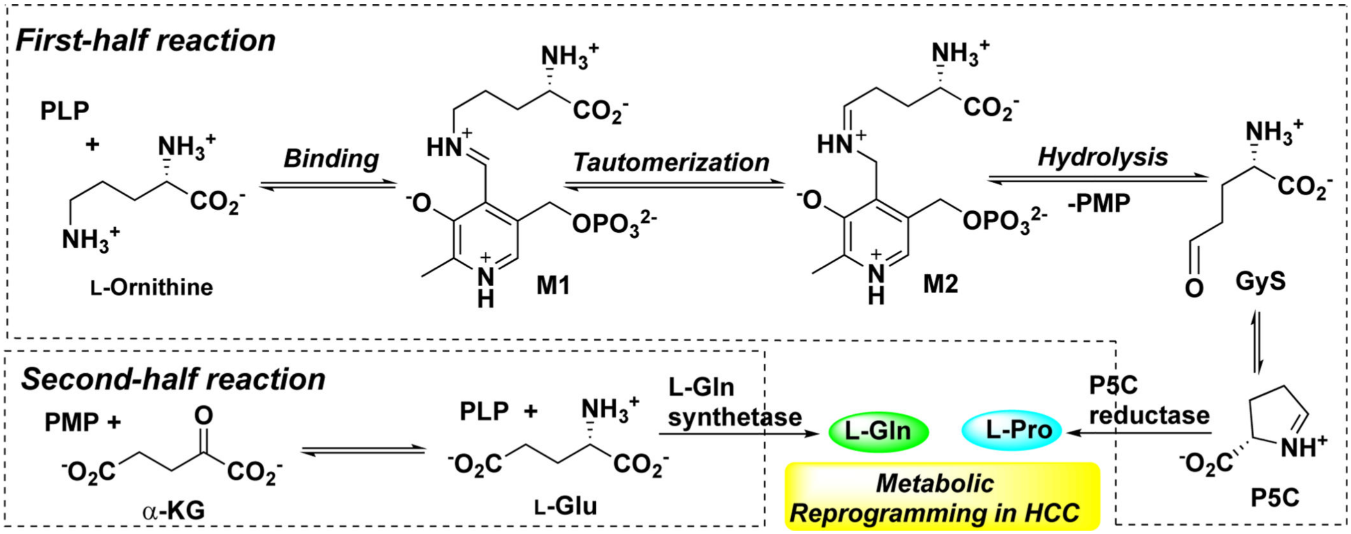

Scheme 1.

Catalytic Mechanism of OAT

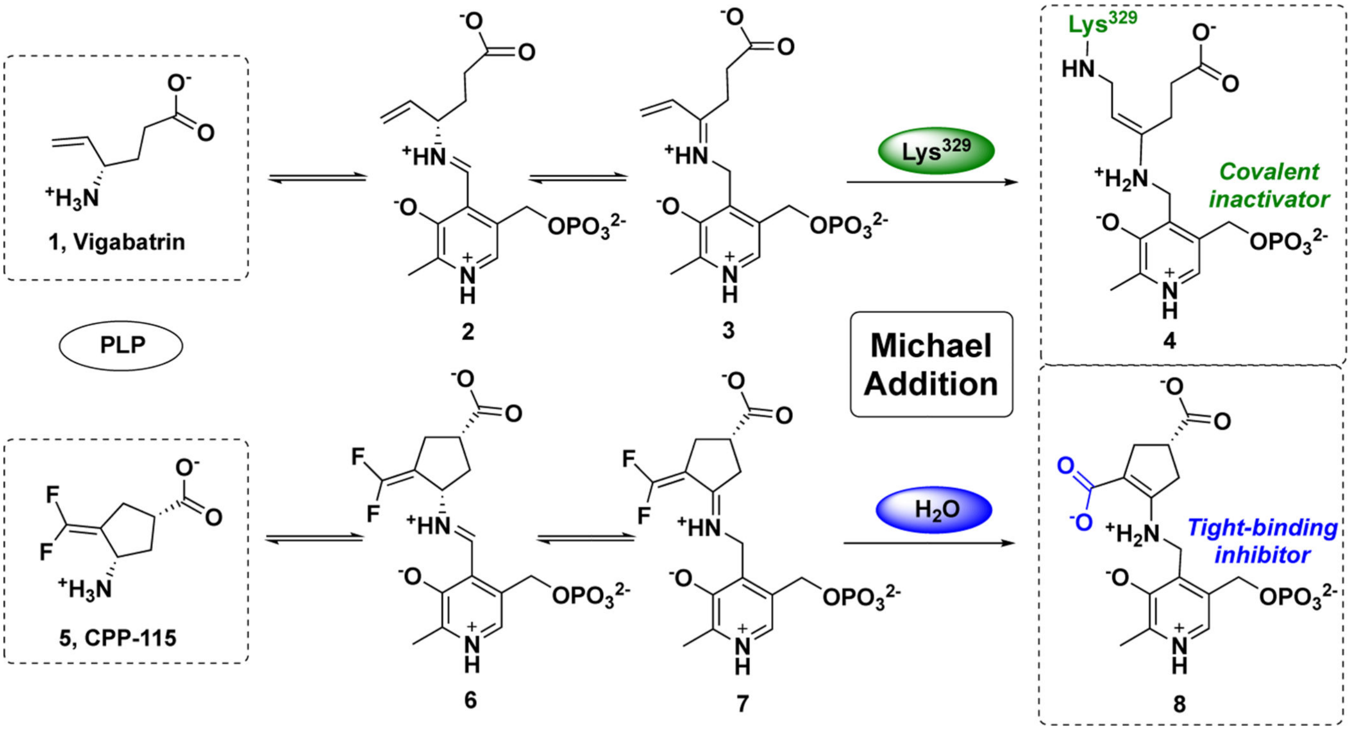

Scheme 2.

Inactivation mechanisms of GABA-AT by vigabatrin (**1**) and CPP-115 (**5**)

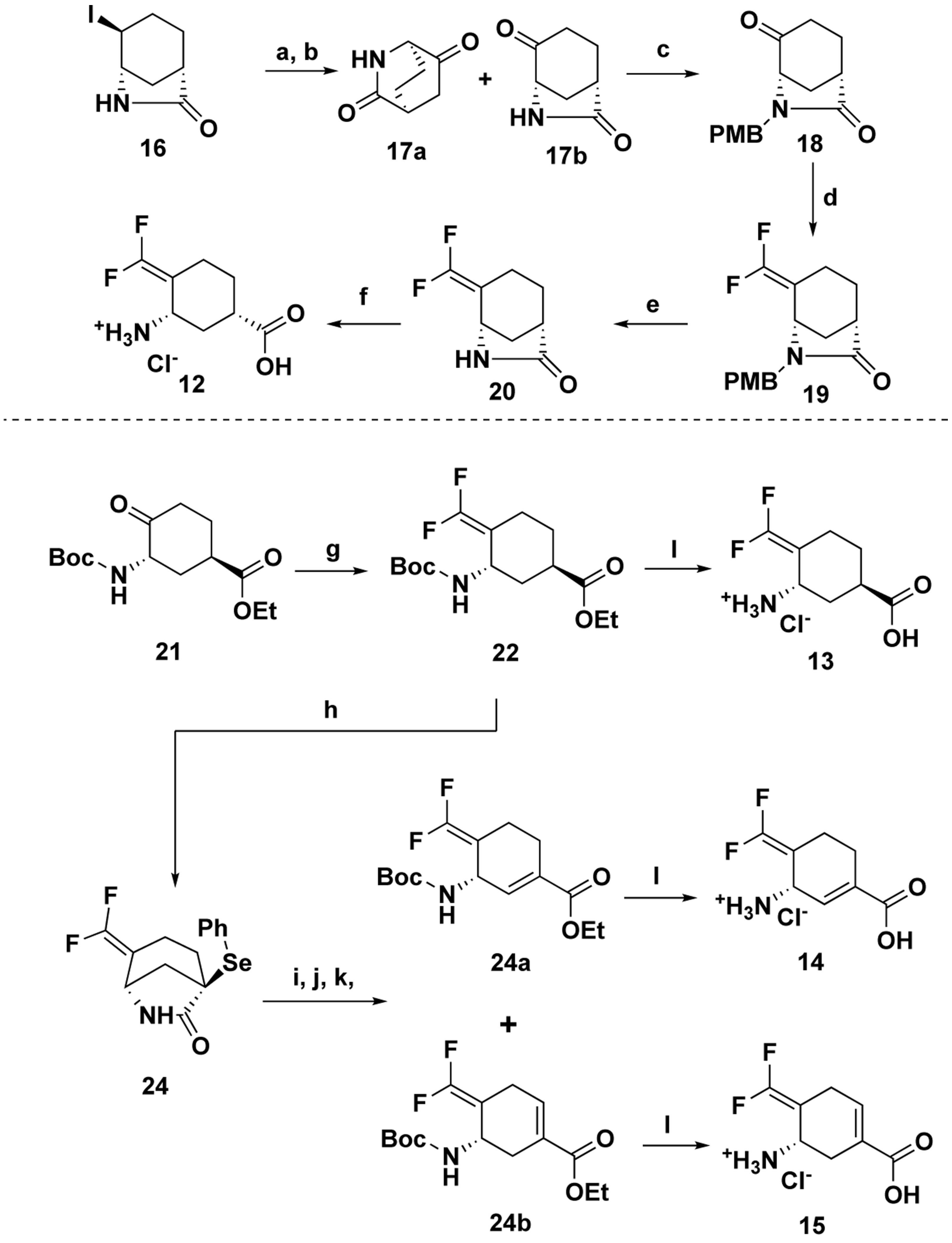

Scheme 3.

Syntheses of six-membered ring analogs **12–15**

Reagents and conditions: (a) AgOC(O)CF$_3$, CH$_3$NO$_2$, 0 °C – r.t., 16h; then NH$_3$/MeOH, 1 h; (b) DMP, CH$_3$CN, NaHCO$_3$ (b) NaH, DMF; PMBCl, 0 °C – r.t., 16h; (c) CHF$_2$PO(OEt)$_2$, ^{t}BuLi (1.7 M in pentane), −100 °C – r.t., 2h; then reflux, 16h; (d) CAN, CH$_3$CN, H$_2$O, 0 °C - r.t., 10 h; (e) HCl (aq. 4 M), 75 °C, 5h. (e) 2-PySO$_2$CF$_2$H, ^{t}BuOK, DMF −60 °C, then −40 °C, 2h, NH$_4$Cl (saturated aq.), HCl (3M), overnight; (f) PhSeCl, KHMDS (1M in THF), −78

°C – r.t., 3h; (g) Boc_2O, DIPEA, DMAP, DCM, r.t., overnight; (h) K_2CO_3, EtOH, 0 °C - r.t. 3h; (i) *m*-CPBA, DCM, r.t., 3h; (j) HCl (aq. 4 M), AcOH, 80 °C, overnight.

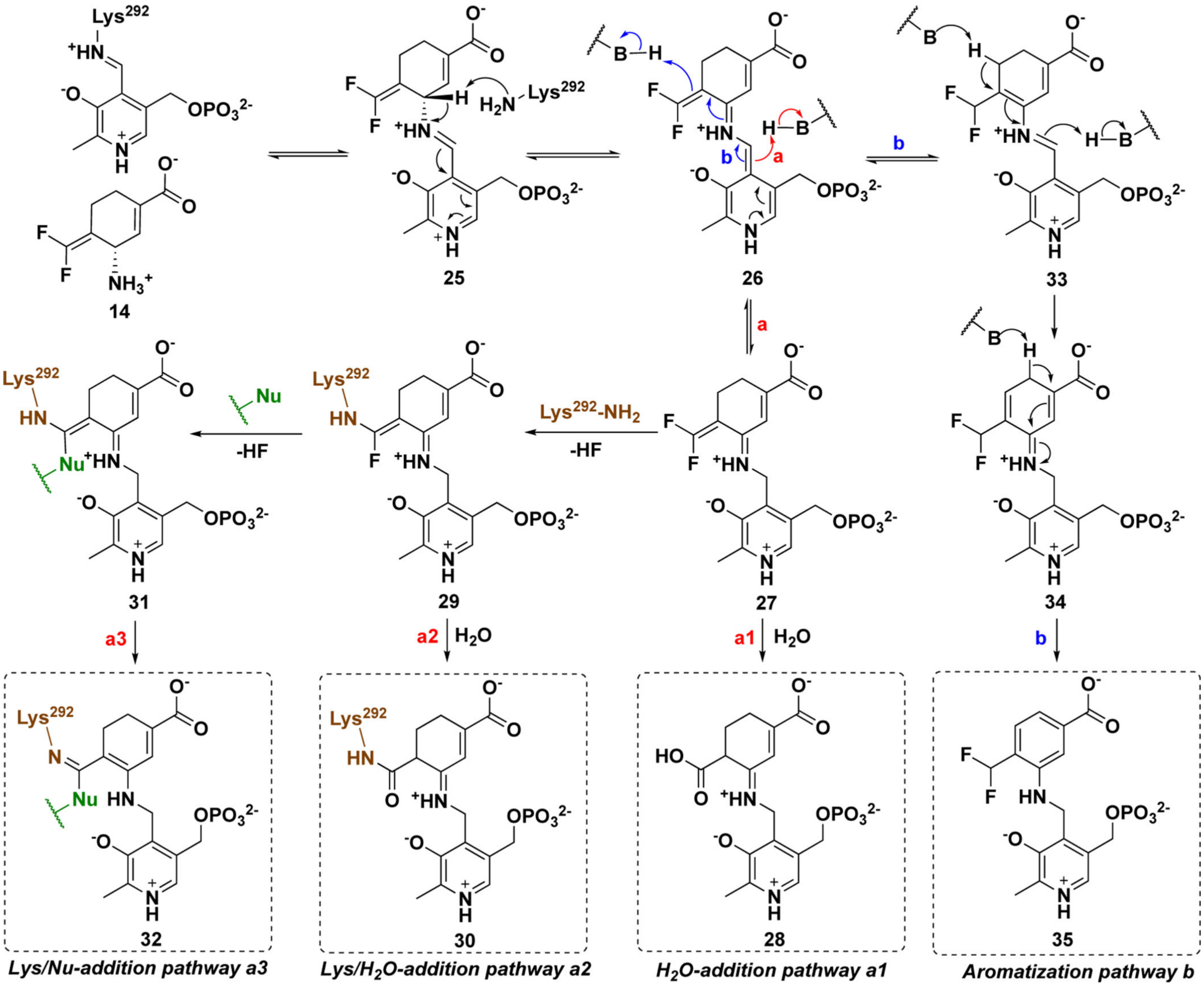

Scheme 4.

Possible inactivation mechanisms for **14**

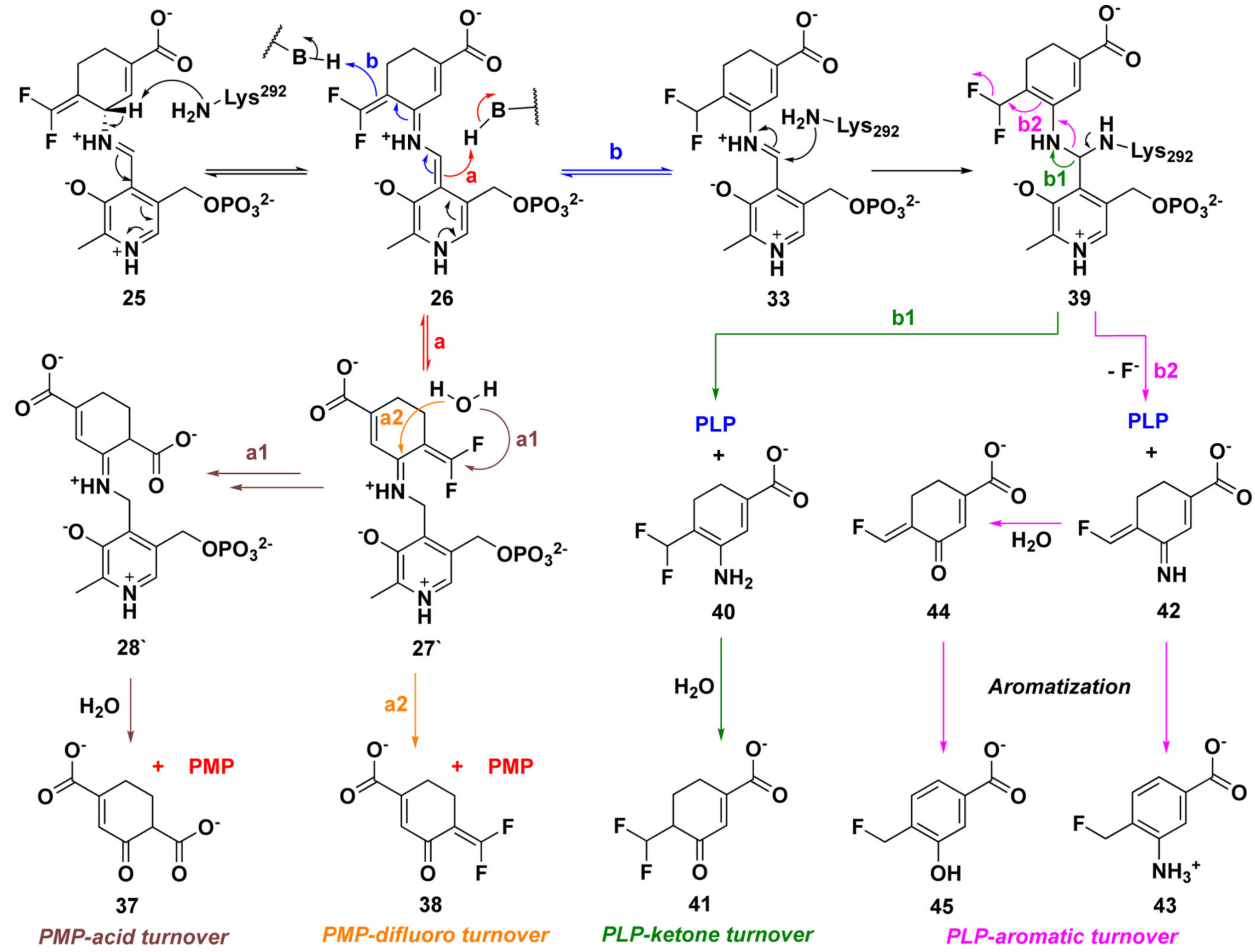

Scheme 5.

Possible turnover mechanisms for **14** by *h*OAT

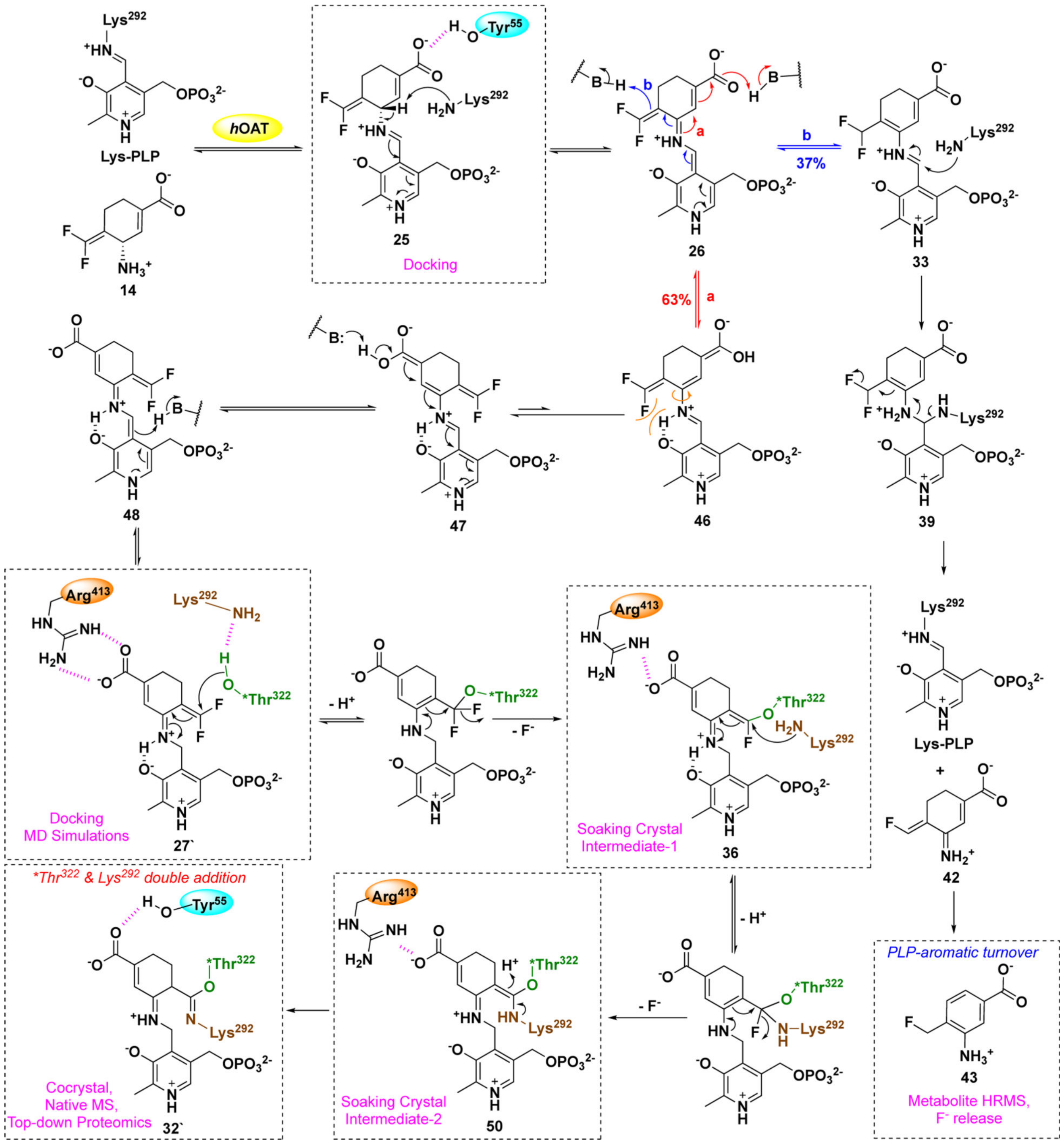

Scheme 6.

Plausible mechanism for **14** with *h*OAT

Table 1.

Kinetic constants for the inactivation of *h*OAT and GABA-AT by **1**, **5**, **9**, **10,** and **12–15**[a]

Comp.	***h*OAT**			**GABA-AT**		
	K_I (mM)	**k_{inact} (min^{-1})**	**k_{inact}/K_I ($mM^{-1}min^{-1}$)**	**K_I (mM)**	**k_{inact} (min^{-1})**	**k_{inact}/K_I ($mM^{-1}min^{-1}$)**
12	1.3 ± 0.2	0.1 ± 0.007	0.08	1.3 ± 0.4	0.03 ± 0.002	0.02
13	1.5 ± 0.2	0.1 ± 0.005	0.07	> 13.1	>0.2	0.02 ± 0.001[b]
14	0.01 ± 0.002	0.2 ± 0.01	20.0	> 1.2	> 0.4	0.3 ± 0.01[b]
15	0.1 ± 0.01	0.05 ± 0.002	0.5	> 2.5	> 0.2	0.09 ± 0.003 [b]
5 [29]	0.12	0.1	0.8	0.06	2.1	34.9
9 [29]	0.003	0.03	7.6	0.01	3.3	342
10 [40]	0.07	0.06	0.9	-	-	-
1 [40]	-	-	-	0.3	0.2	0.7

[a] k_{inact} and K_I values were determined by the equation: $k_{obs} = k_{inact}*[I]/(K_I + [I])$ and are presented as means and standard errors.

[b] The ratio of k_{inact}/K_I was determined by the slope of $k_{obs} = k_{inact}*[I]/(K_I + [I])$. k_{inact} is greater than the maximum k_{obs} determined in the time-dependent assay; K_I is greater than k_{obs}(max)/the ratio of k_{inact}/K_I.

Table 2.

The mass differences for the proposed adducts between theoretical and experimental mass values of native/modified *h*OAT observed in native MS.

Samples	Theoretical mass difference (per monomer, Da)	Experimental mass (dimer, Da)	Experimental mass difference (per monomer, Da)
Native *h*OAT	231.0	92736.6 ± 1.8	**230.8**
*h*OAT- gabaculine	368.1	93014.8 ± 1.5	**369.9**
*h*OAT-**11b**	366.1	93009.2 ± 1.0	**367.1**
*h*OAT-**14**	414.1 (**28** in pathway *a1*) 396.1 (**30** in pathway *a2*) 378.1 (**32** in pathway *a3*) 418.1 (**35** in pathway *b*)	93031.6 ± 0.9	**378.3**

Table 3.

Fluoride ion release during different turnover pathways with and without α-KG

Conditions	Pathway *a1*	Pathway *a2*	Pathway *b1*	Pathway *b2*	Experimental
With *α*-KG	3.2 equiv	2.0 equiv	2.0 equiv	2.6 equiv	**2.9 equiv**
Without α-KG	2.0 equiv	1.3 equiv	2.0 equiv	2.6 equiv	**2.7 equiv**